First-Principles Thermal Conductivity of Deuterium for Inertial Confinement Fusion Applications

Introduction

As a grand challenge to harvest the "ultimate" energy source in a controlled fashion, inertial confinement fusion (ICF)[1] has been actively pursued for decades using both indirect-drive[2,3] and direct-drive[4–6] configurations. Understanding and designing ICF capsule implosions rely on simulations using multi-physics radiation–hydrodynamics codes, in which each piece of the physics models must be accurate. According to the ICF ignition criterion,[7,8] the minimum laser energy required for ignition scales as

$$E_{\mathrm{L}}(\mathrm{kJ}) \simeq 590 \times \alpha^{1.9} \times \left(\frac{3 \times 10^7}{V_{\mathrm{imp}}} \right)^{6.6} \times \left(\frac{P_{\mathrm{a}}}{100\ \mathrm{Mbar}} \right)^{-0.8}, \quad (1)$$

where the implosion velocity V_{imp} is in cm/s, P_{a} is the ablation pressure in Mbar, and the DT shell's adiabat α is conventionally defined as $\alpha = P/P_{\mathrm{F}}$, the ratio of plasma pressure to the Fermi-degeneracy pressure (P_{F}). This scaling law indicates that the lower the shell adiabat, the less energy needed for ignition. For lower-α implosions, however, the DT shell is in the regime in which strong coupling and degeneracy plasma effects are important and must be taken into account for meaningful implosion modeling.

The determination of accurate plasma properties is also very important for understanding low-adiabat ($\alpha \leq 2$) ICF implosions. Precise knowledge of the static and dynamic properties of ICF target materials, including ablators and the deuterium–tritium (DT) fuel, is required under high-energy-density conditions. For instance, the equation of state (EOS) of the target materials determines how much compression can be attained under external pressures generated by x-ray/laser ablations.[9] For this exact reason, state-of-the-art EOS experiments and calculations have been performed for ICF-relevant materials[10–16] over the past few years. The theoretical approaches have employed first-principles methods such as the path-integral Monte Carlo (PIMC),[17] coupled electron–ion Monte Carlo (CEIMC),[18] and quantum molecular dynamics (QMD)[19] based on the finite-temperature density-functional theory. Besides static EOS information, the dynamic transport properties of relevant materials are in high demand for accurate ICF simulations. Transport and optical properties (thermal and electrical conductivities) of DT and ablators not only affect the thermal conduction, but also determine the radiation transport in the imploding shell.

Soon after the introduction of the ICF concept[1] in 1972, studies followed to determine the most-appropriate models for thermal conductivity of strongly coupled and degenerate plasmas in the high-density, low-temperature regime.[20] The Spitzer model[21] of thermal conductivity κ, formulated in the 1950s for ideal plasmas, breaks down in this regime since the Coulomb logarithm[22–26] for electron–ion collisions becomes negative. Brysk *et al.*[20] suggested in the 1970s that the Hubbard model[27] of degenerate plasma be "bridged" with the Spitzer model.[21] In the 1980s, Lee and More[28] applied Krook's model to the Boltzman equation and derived a set of transport coefficients, including κ. Meanwhile, Ichimaru and colleagues[29] developed the so-called "Ichimaru model" of thermal conductivity for fully ionized plasmas using the linear response theory. In addition, the average-atom model[30] and its improved versions have been used to numerically calculate κ for materials of interest to ICF and astrophysics, with tools such as the PURGATORIO package[31] and the SCAALP model.[32] As a result of recent progress in the *first-principles* method of quantum molecular dynamics,[33–37] these various thermal-conductivity models of hydrogen/DT have been tested against QMD calculations.[38–43] For ICF stagnation plasma conditions near peak compression, the pioneering QMD calculations by Recoules *et al.*[38] have shown an orders-of-magnitude increase in κ for the coupled and degenerate regimes when compared with the extensively used Lee–More model[28] for a corresponding deuterium density of $\rho_{\mathrm{D}} \simeq 160\ \mathrm{g/cm}^3$.

These recent studies have motivated us to investigate how the more-accurate results of thermal conductivity κ derived from QMD calculations could affect the hydrodynamic pre-

dictions of ICF implosions. Apparently, the change in κ for ablator materials[40] (CH, Be, or C) can enhance heat flow into the cold shell from the hot coronal plasma. This may modify the mass ablation rate, thereby altering the implosion velocity. Data over a wide range of density and temperature conditions do not currently exist from QMD calculations of κ for ICF ablator materials. The effects of updated ablator thermal conductivities on ICF target performance are left for future studies. Here, we focus on how the QMD-calculated κ of DT fuel might affect ICF simulations. Recently, Lambert *et al.*[39] extended their original QMD calculations of κ_{DT} for three different densities of $\rho_{DT} = 25$, 200, and 400 g/cm^3. They argued that the variation of κ_{DT} can change the thermodynamical path to ignition by modifying the ablation process at the boundary between the hot core and the dense cold shell. Under similar circumstances, Wang *et al.*[43] also computed κ_{DT} for several other high-density points of $\rho_{DT} = 200$ to 600 g/cm^3, using the QMD simulation package *ABINIT*.[44] They briefly discussed the effect of κ variations on hydrodynamic simulations based solely on their high-density QMD results.

As we have shown previously,[45] an imploding DT shell undergoes a wide range of densities from $\rho_{DT} \simeq 1.0$ g/cm^3 at the shock transit stage and $\rho_{DT} \simeq 5.0$ to 10.0 g/cm^3 during in-flight shell acceleration, up to $\rho_{DT} \geq 300$ g/cm^3 at stagnation (i.e., at peak compression). To cover all the relevant density points in ICF, we have performed QMD calculations of the thermal conductivity κ through the usual Kubo–Greenwood formulation[46] by spanning deuterium densities from $\rho \simeq 1.0$ g/cm^3 to $\rho \simeq 673.5$ g/cm^3 at temperatures varying from $T = 5000$ K to $T = 8,000,000$ K. We have compared the calculated κ_{QMD} with the following "hydrid" thermal-conductivity model currently used in our hydrocode *LILAC*:[47]

$$\kappa_{LILAC} = \frac{20 \times (2/\pi)^{3/2} k_B^{7/2} T^{5/2}}{\sqrt{m_e} Z_{eff} e^4} \times \frac{0.095 \times (Z_{eff} + 0.24)}{1 + 0.24 Z_{eff}}$$

$$\times \frac{1}{[\ln\Lambda]_{LM}} \times f_{LM}(\rho,T). \qquad (2)$$

In this hybrid model of κ_{LILAC}, the Spitzer prefactor is used in combination with the replacement of the Spitzer Coulomb logarithm by that of Lee and More, $[\ln\Lambda]_{LM}$. In addition, the Lee–More degeneracy correction function $f_{LM}(\rho,T)$ has been adopted in the following form:

$$f_{LM}(\rho,T) = 1 + \frac{3\pi^5}{51,200} \times \left(\frac{T_F}{T}\right)^3$$

$$\times \left[\frac{1 + 0.24 Z_{eff}}{0.095 \times (Z_{eff} + 0.24)}\right]^2, \qquad (3)$$

where $T_F = (\hbar^2/2m_e k_B)(3\pi^2 n_e)^{2/3}$ is the Fermi temperature of the electrons in a fully ionized plasma, k_B is the Boltzmann constant, and m_e and n_e are the mass and number density of electrons. The effective charge of ions is defined as $Z_{eff} = \langle Z^2 \rangle / \langle Z \rangle$ averaging over the species ($Z_{eff} = 1$ for fully ionized DT plasmas). In general, our QMD results showed a factor-of-3 to 10 enhancement in κ_{QMD} over κ_{LILAC} within the ICF-relevant density and temperature ranges.

To test the effects of κ_{QMD} on ICF implosions, we have fitted the calculated κ_{QMD} with a fifth-order polynomial function of the coupling parameter $\Gamma = 1/(r_S k_B T)$ and the degeneracy parameter $\theta = T/T_F$. The Wigner–Seitz radius r_S is related to the electron number density $n_e = 3/(4\pi r_S^3)$. The fitted formula of κ_{QMD} is then applied in *LILAC* to simulate a variety of cryogenic DT implosions on OMEGA as well as direct-drive designs at the National Ignition Facility (NIF). Compared with simulations using κ_{LILAC}, we found variations of up to ~20% in the target-performance predictions using the more-accurate κ_{QMD}. The lower the adiabat of imploding shells, the stronger the coupling and degeneracy effects of κ_{QMD}.

This article is organized as follows: The QMD method is described briefly in the next section, which also examines other methods and experiments on deuterium plasma properties; the calculated κ_{QMD} of deuterium for a wide range of density and temperature points is presented and compared with κ_{LILAC}; the κ_{QMD} effects on ICF implosion dynamics are discussed in detail, followed, in the final section, by the summary.

The Quantum Molecular Dynamics Method

We have used the QMD method for simulating warm, dense deuterium plasmas. Since the QMD procedures have been well documented elsewhere,[34,48–50] we present only a brief description of its basics. The Vienna *ab-initio* Simulation Package (VASP)[51,52] has been employed within the isokinetic ensemble (number of particles, volume, and temperature constant). VASP is based on the finite-temperature density-functional theory (FTDFT). Specifically, the electrons are treated quantum mechanically by plane-wave FTDFT calculations using the

Perdew-Burke-Ernzerhof generalized gradient approximation (GGA) for the exchange-correlation term. The electron–ion interaction was modeled by either a projector argumented wave (PAW) pseudopotential[53] or the pure Coulombic potential. The system was assumed to be in local thermodynamic equilibrium with equal electron and ion temperatures ($T_e = T_i$). The ion temperature was kept constant by simple velocity scaling.

A periodically replicated cubic cell was used with equal numbers of electrons and deuterium ions. The plasma density and the number of D atoms determined the volume of the cell. For the present simulations of densities below $\rho_D = 15.7$ g/cm³, we employed 128 atoms and the PAW pseudopotential. For high densities ($\rho_D \geq 15.7$ g/cm³), a varying number of atoms ($N = 216$ to 1000) were used and incorporated with the pure Coulombic potential.[54] For each molecular dynamics (MD) step, a set of electronic state functions for each k point was self-consistently determined for an ionic configuration. Then, the ions were moved classically with a velocity Verlet algorithm according to the combined ionic and electronic forces. Repeating the two steps propagated the system in time, resulting in a set of self-consistent ion trajectories and electronic state functions. These trajectories provide a consistent set of static, dynamical, and optical properties of the deuterium plasmas.

All of our QMD calculations employed only a Γ-point ($\mathbf{k} = 0$) sampling of the first Brillouin zone in the cubic cell; such a sampling has been shown to produce properties of sufficient accuracy in this regime.[39,43] For low-density points, a tight PAW pseudopotential was used with a maximum energy cutoff of $E_{max} = 700$ eV to avoid core overlap. The Coulombic potential for high-density points had a cutoff energy varying from $E_{max} = 1000$ eV to $E_{max} = 8000$ eV. A large number of energy bands N_b (up to 3500) were included to ensure high accuracy (the lowest population down to a level of 10^{-5}). To benchmark our current QMD calculations, we first compare the EOS results with previous PIMC calculations[11] for a deuterium density of $\rho_D = 5.4$ g/cm³. Both the QMD calculation using PAW pseudopotential and the PIMC simulation used 128 atoms in the cell. The total pressure is a sum of the electronic pressure (averaging over the MD times) and the classical ionic pressure; the internal energy is referenced to the ground-state energy ($E_0 = -15.9$ eV) of a D_2 molecule. The EOS results shown in Fig. 137.63 demonstrated excellent agreement within the overlapping temperature range where both methods are valid. In addition, we have also performed convergence tests of QMD calculations by using the Coulombic potential and more atoms ($N = 343$) for this density. The results are plotted
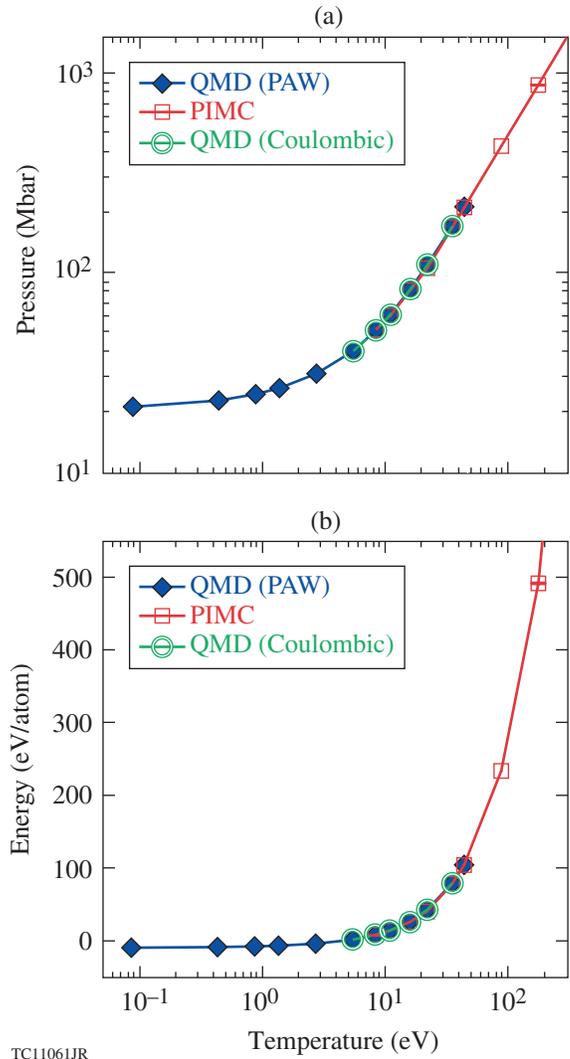

Figure 137.63
The equation-of-state comparison between quantum molecular dynamics (QMD) and path-integral Monte Carlo (PIMC) calculations for deuterium density at $\rho = 5.4$ g/cm³: (a) pressure versus temperature and (b) internal energy versus temperature. PAW: projector-argumented wave.

by green open circles in Fig. 137.63, which are almost identical to the PAW calculations.

To calculate the electron thermal conductivity of a plasma, we consider the linear response of the plasma to an electric field $\mathbf{E}$ and a temperature gradient ∇T, which induce the electric current $\mathbf{j}_e$ and the heat flux $\mathbf{j}_q$:

$$\mathbf{j}_e = \left(eL_{11}\mathbf{E} - \frac{L_{12}\nabla T}{T} \right) \Big/ e, \tag{4}$$

$$\mathbf{j}_q = \left(eL_{21}\mathbf{E} - \frac{L_{22}\nabla T}{T}\right)\bigg/e. \quad (5)$$

For plasmas having no electric current ($\mathbf{j}_e = 0$), the above equations in combination with the definition of $\mathbf{j}_q = -\kappa\nabla T$ give the thermal conductivity

$$\kappa = \frac{1}{T}\left(L_{22} - \frac{L_{12}^2}{L_{11}}\right) \quad (6)$$

with the Onsager coefficients given by L_{ij}. In the absence of temperature gradient ($\nabla T = 0$), Eq. (4) reduces to Ohm's law with the electrical conductivity of $\sigma = L_{11}$. The frequency-dependent Onsager coefficients can be calculated using the Kubo–Greenwood formalism:[46]

$$L_{ij}(\omega) = \frac{2\pi(-e)^{4-i-j}}{3Vm_e^2\omega}\sum_{m,n}F_{mn}\left|D_{mn}\right|^2$$

$$\times\left(\frac{E_m + E_n}{2} - H\right)^{i+j-2}\delta\left(E_m - E_n - \hbar\omega\right), \quad (7)$$

where V is the atomic volume, $E_m(E_n)$ is the energy of the mth (nth) state, and H is the enthalpy (per atom) of the system. The quantity of F_{mn} is the difference between the Fermi–Dirac distributions for the involved states m and n at temperature T. The velocity dipole matrix elements D_{mn} can be computed from the VASP wave functions. In practical calculations, the

δ function in Eq. (7) is approximated by a Gaussian function of width ΔE ($\simeq 0.1$ to 0.5 eV). In addition, $L_{ij} \equiv L_{ij}(0)$ is used in Eq. (6). The resulting κ was averaged over at least ten snapshots of uncorrelated configurations along the MD trajectories. The determination of κ required, for convergence, a much larger number of energy bands ($\sim 3\times$) than for the MD simulation.

Since no direct measurements exist for the thermal conductivity in deuterium plasmas, we compared our QMD calculations to a related optical property, the reflectivity, which has been determined along the principal Hugoniot in shock-timing experiments[55–58] using the velocity interferometer system for any reflector (VISAR). The reflectivity is determined by

$$R(\omega) = \frac{\left[1 - n(\omega)\right]^2 + k(\omega)^2}{\left[1 + n(\omega)\right]^2 + k(\omega)^2}, \quad (8)$$

with the real and imaginary parts of refraction indices $[n(\omega), k(\omega)]$ that can be computed from the dielectric function of $\epsilon(\omega) = \epsilon_1(\omega) + i\epsilon_2(\omega)$. The dielectric functions are obtained from the real electric conductivity $\sigma_1(\omega) = L_{11}(\omega)$ and its imaginary part $\sigma_2(\omega)$ determined by a principal-value integral of $\sigma_1(\omega)$. In Fig. 137.64, the calculated reflectivities of deuterium as a function of shock speed for different VISAR wavelengths are compared with both Nova[55] and recent OMEGA measurements along the principal Hugoniot. The OMEGA experiments were taken from a decayed shock in deuterium over many shots. This experimental confirmation, together with agreement with
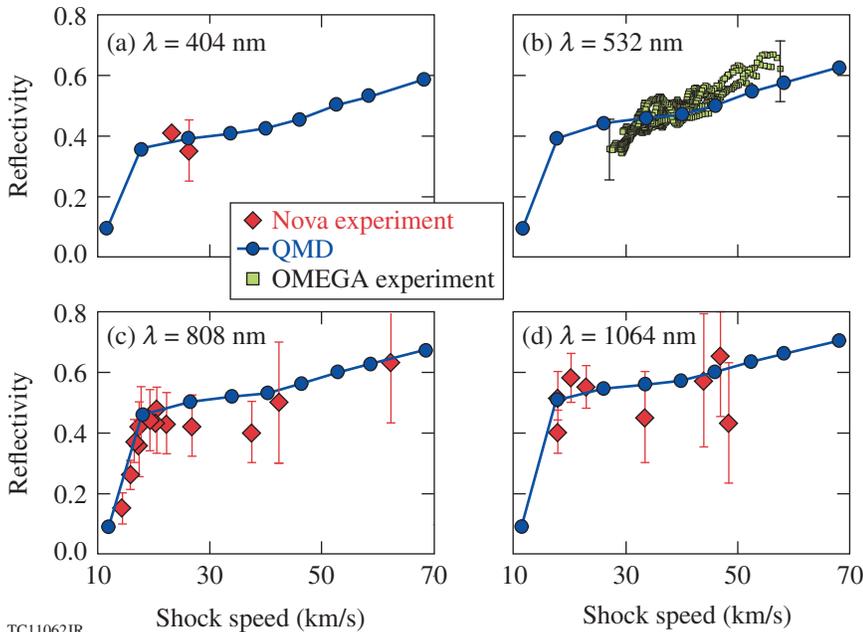

TC11062JR

Figure 137.64
The QMD-calculated reflectivity of deuterium shock as a function of shock speed along the principal Hugoniot, which is compared to both a previous Nova measurement[55] and a recent OMEGA experiment for different VISAR wavelengths: (a) $\lambda = 404$ nm, (b) $\lambda = 532$ nm, (c) $\lambda = 808$ nm, and (d) $\lambda = 1064$ nm.

other first-principle results,[59] lends credence to the L_{11} coefficients produced in this study and, in turn, to the other similarly calculated Onsager coefficients that determine κ.

Thermal Conductivity of Deuterium for a Wide Range of Densities and Temperatures

The QMD calculations of deuterium thermal conductivity have been performed for a wide range of densities [$\rho = 1.0$ to 673.5 g/cm^3], at temperatures varying from $T = 5000$ K to $T = 8,000,000$ K. For each density point, the κ_{QMD} calculations have been performed to the highest temperature approaching $T \simeq T_F$. (Tabulated results of κ_{QMD} are found in the **Supplementary Material**, p. 92.) To test the effects of κ_{QMD} on ICF implosions, we have fitted the κ_{QMD} results to the following function (in a similar format of κ_{LILAC}):

$$\kappa_{QMD} = \frac{20 \times (2/\pi)^{3/2} k_B^{7/2} T^{5/2}}{\sqrt{m_e} Z_{eff} e^4}$$

$$\times \frac{0.095 \times (Z_{eff} + 0.24)}{1 + 0.24 Z_{eff}} \times \frac{1}{(\ln\Lambda)_{QMD}}, \quad (9)$$

with the same Spitzer prefactor as used in κ_{LILAC} and $Z_{eff} = 1$. The generalized QMD Coulomb logarithm has the following form:

$$(\ln\Lambda)_{QMD} = \exp\left\{ \alpha_0 + \sum_{i=1}^{5} \left[\alpha_i (\ln\Gamma)^i + \beta_i (\ln\theta)^i \right] \right\}. \quad (10)$$

This fifth-order polynomial function of coupling and degeneracy parameters (Γ, θ) has been fitted to the κ_{QMD} data using multivariable least-squares fitting. To make κ_{QMD} converge to κ_{LILAC} at the ideal plasma conditions ($\Gamma \ll 1$ and $\theta \gg 1$), we have added the high-temperature points of κ_{LILAC} into the data set for the global fitting. The resulting fitting parameters are:

$$
\begin{aligned}
\alpha_0 &= -0.74015 \\
\alpha_1 &= -0.18146 \\
\alpha_2 &= +6.39644\,E{-}004 \\
\alpha_3 &= +1.47954\,E{-}003 \\
\alpha_4 &= -1.23362\,E{-}004 \\
\alpha_5 &= -2.58107\,E{-}005 \\
\beta_1 &= +0.86155 \\
\beta_2 &= -0.10570 \\
\beta_3 &= -6.75783\,E{-}003 \\
\beta_4 &= -1.69007\,E{-}004 \\
\beta_5 &= +3.49201\,E{-}004
\end{aligned}
\quad (11)
$$

The fit results of $(\ln\Lambda)_{QMD}$ are plotted in Figs. 137.65(a) and 137.65(b) as a function of $\ln(\Gamma)$ and $\ln(\theta)$, respectively. Overall,
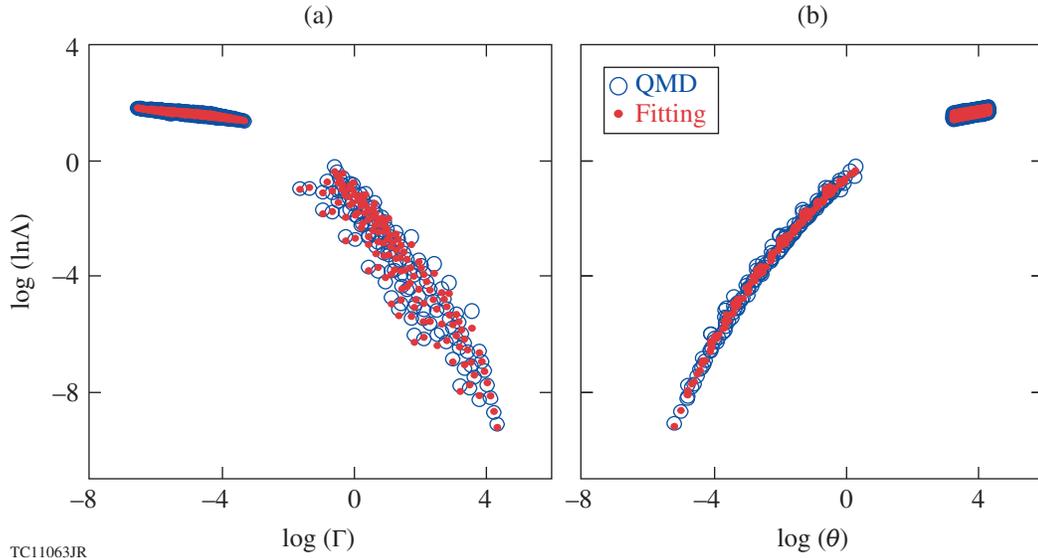

Figure 137.65
The generalized Coulomb logarithm, derived from QMD-calculated thermal conductivities for different densities and temperatures, is fitted with the polynomial function [Eq. (10)] of (a) the coupling parameter (Γ) and (b) the degeneracy parameter (θ). The values of $\ln\Lambda$ at high temperatures [i.e., log($\ln\Lambda$) > 0] are converged to the standard *LILAC* values.

the global fitting with the above parameters gives only a small error of ~5%.

Comparisons of κ_{QMD} with κ_{LILAC} are plotted in Figs. 137.66 and 137.67 for deuterium densities of ρ = 2.5, 10.0, 43.1, and 199.6 g/cm^3. The green dashed lines represent the thermal con-ductivity currently used in our hydrocode *LILAC*, while the blue solid triangles represent the QMD results. The red solid line is the QMD fit discussed above. We observe that κ_{QMD} is higher than κ_{LILAC} by a factor of 3 to 10 in the coupled and degenerate regimes ($\Gamma > 1$, $\theta < 1$). The QMD-fit line merges into κ_{LILAC} at a high-T regime ($T > 10\,T_F$), as expected.
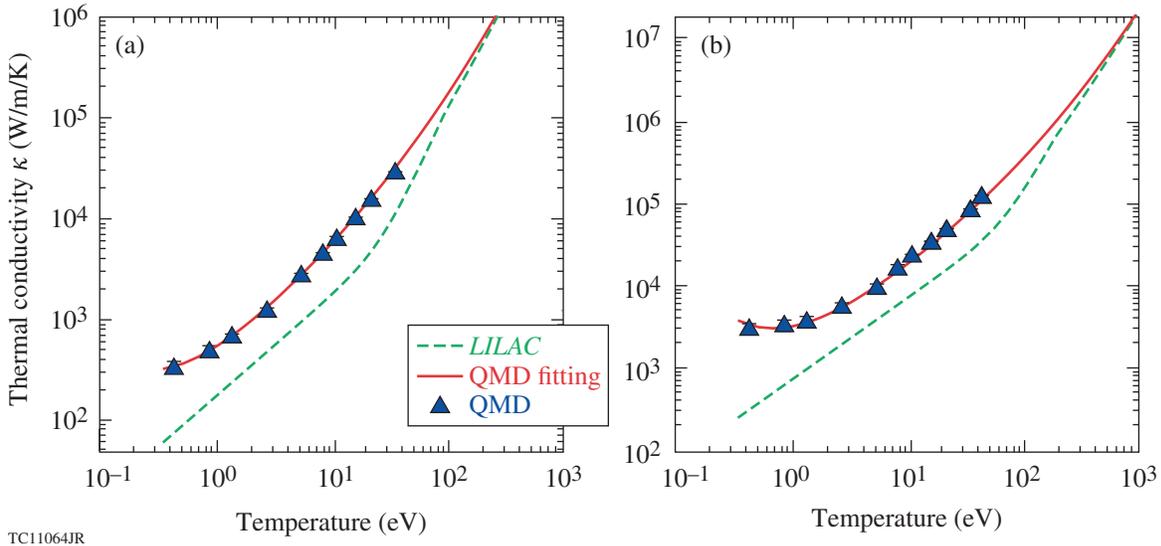

TC11064JR

Figure 137.66
The thermal conductivities from first-principles QMD calculations, the QMD-fitting formula [Eq. (10)], and the hybrid model used in *LILAC* are plotted as a function of temperature for deuterium densities of (a) ρ = 2.5 g/cm^2 and (b) ρ = 10.0 g/cm^2.
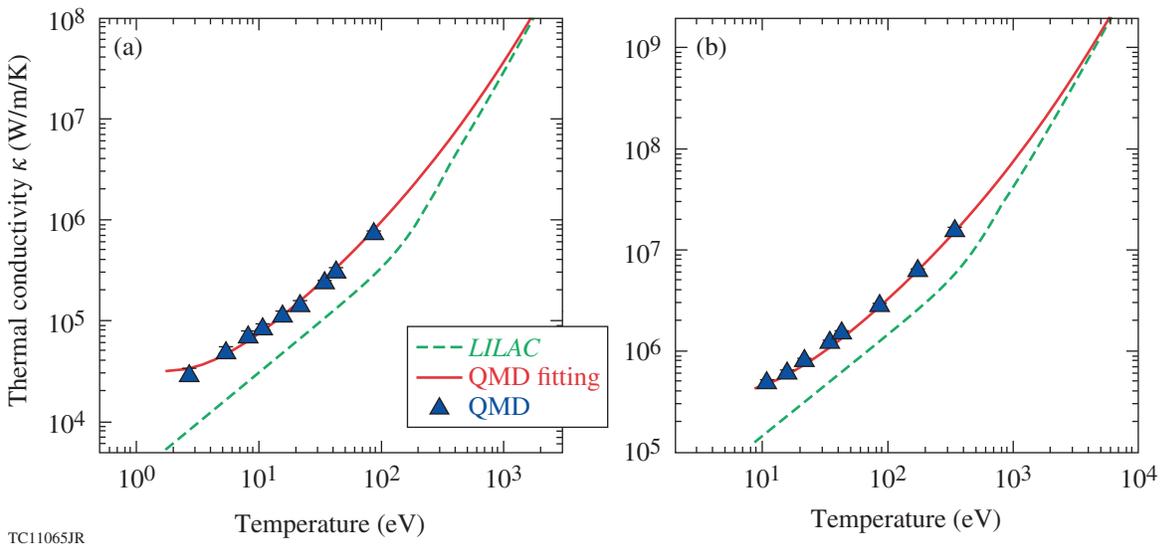

TC11065JR

Figure 137.67
The thermal conductivities from first-principles QMD calculations, the QMD-fitting formula [Eq. (10)], and the hybrid model used in *LILAC* are plotted as a function of temperature for deuterium densities of (a) ρ = 43.1 g/cm^2 and (b) ρ = 199.6 g/cm^2.

Effects of κ_{QMD} on ICF Implosions

To test how the QMD-predicted thermal conductivity of DT affects ICF implosions, we have incorporated the κ_{QMD} fit into our one-dimensional (1-D) radiation−hydrocode *LILAC*. The hydrodynamic simulations employed the flux-limited thermal conduction model[60–63] with a flux limiter of $f = 0.06$. Two cryogenic DT target implosions on OMEGA and three NIF direct-drive designs have been examined. These ICF implosions span a wide range of implosion velocities and adiabats. The adiabat (α) characterizes the plasma degeneracy degree of the imploding DT shell: the lower the adiabat, the more degenerate the DT plasma.

First, we show simulations of two cryogenic DT implosions on OMEGA in Figs. 137.68 and 137.69. A typical OMEGA cryogenic DT target has a diameter of ~860 μm, which consists of a plastic ablator with a thickness of 8 to 11 μm and a layer of 45 to 65 μm of DT ice. In Fig. 137.68(a), the laser pulse has a relatively high first picket, which sets up the DT shell in a high adiabat of $\alpha \simeq 4$. The density and ion temperature profiles at the peak compression are plotted in Fig. 137.68(b). The blue dashed line represents the case of using standard κ_{LILAC} in the simulation, while the red solid line represents the κ_{QMD} simulation. Figure 137.68(b) shows that there is little change in the target performance for this high-adiabat implosion. In the end, the neutron yields are predicted to be 3.32×10^{14} (κ_{LILAC}) and 3.24×10^{14} (κ_{QMD}) for the two cases.

Predictions for the low-adiabat ($\alpha \simeq 2.2$) implosion are shown in Fig. 137.69. Figure 137.69(a) plots the laser pulse used for this OMEGA implosion. The in-flight plasma conditions are illustrated in Fig. 137.69(b) at $t = 2.7$ ns, just before stagnation, in which the mass density and electron temperature are drawn as a function of the target radius. Noticeable differences in electron-temperature profiles are seen for the two cases using κ_{QMD} and κ_{LILAC}; the peak density changed slightly when κ_{QMD} was used. These differences can affect the target performance at stagnation ($t = 2.84$ ns), as shown by Fig. 137.69(c). Finally, Fig. 137.69(d) indicates that the neutron yield is ~6% lower in the κ_{QMD} simulation than for κ_{LILAC}. Table 137.VI summarizes the comparison of other quantities for the two simulations. The neutron-averaged compression ρR and T_i are hardly changed, but the peak density and neutron yield vary by ~6%.

Table 137.VI: Comparison of an OMEGA implosion ($\alpha \simeq 2.2$) predicted using κ_{LILAC} versus κ_{QMD}.

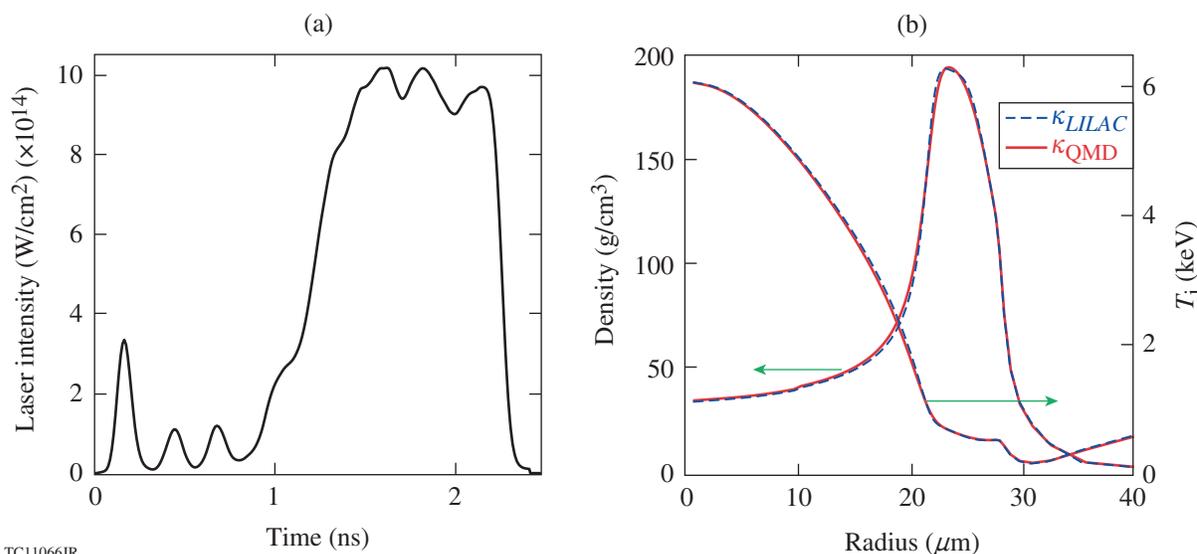|	κ_{LILAC}	κ_{QMD}
$\langle \rho R \rangle_n$	298 mg/cm^2	296 mg/cm^2
$\langle T_i \rangle_n$	4.66 keV	4.64 keV
$\langle P \rangle_n$	197 Gbar	194 Gbar
$\langle \rho \rangle_{peak}$	380.8 g/cm^3	361.7 g/cm^3
Yield	5.34×10^{14}	5.05×10^{14}

(a)

(b)

TC11066JR

Figure 137.68
(a) The laser pulse shape used for a high-adiabat ($\alpha = 4$) cryogenic DT implosion on OMEGA (the $\phi = 868.8$-μm capsule consists of 47 μm of DT ice with an 8.4-μm-thick plastic ablator); (b) comparisons of the density and ion-temperature profiles at peak compression for the two hydrodynamic runs using κ_{LILAC} (blue dashed lines) and κ_{QMD} (red solid lines), respectively. Very little difference is seen in target performance for the two thermal-conductivity models used for such a high-adiabat implosion. Green arrows indicate the vertical axis that applies to each curve.
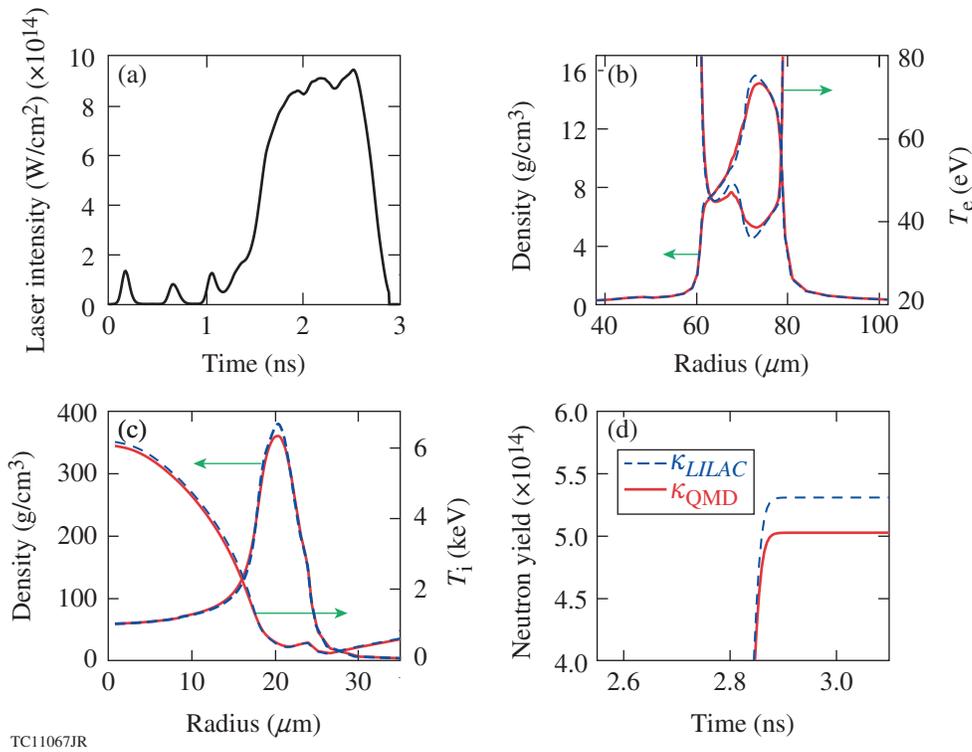
TC11067JR

Figure 137.69
(a) The laser pulse shape used for a low-adiabat ($\alpha = 2.2$) cryogenic DT implosion on OMEGA (the $\phi = 860.6$-μm capsule consists of 49 μm of DT ice with an 8.3-μm-thick plastic ablator). [(b),(c)] Comparisons of the density and temperature profiles at the beginning of the deceleration phase and at peak compression, respectively, for the two hydrodynamic simulations using κ_{LILAC} (blue dashed lines) and κ_{QMD} (red solid lines). (d) The neutron yields as a function of time are plotted for the two cases. A modest variation (~6%) in target performance is seen in such low-adiabat OMEGA implosions, when κ_{QMD} is compared to the hybrid *LILAC* model.

Next we discuss the κ_{QMD} effects on three different direct-drive–ignition designs for the NIF. These NIF designs have slightly different target sizes varying from $\phi = 3294$ μm to $\phi = 3460$ μm. The thickness of the DT-ice layer changes from $d = 125$ μm to $d = 220$ μm; all targets have a plastic ablator at somewhat different thicknesses of 22 to 30 μm. We discuss the κ_{QMD} effects on the performance of three NIF designs from a mid-adiabat ($\alpha = 3.2$) implosion to a very low adiabat ($\alpha = 1.7$) design. Figure 137.70 shows first the mid-adiabat ($\alpha = 3.2$) design: (a) the triple-picket pulse shape (total energy of 1.5 MJ) and (b) the density and ion-temperature profiles at the bang time ($t = 13.78$ ns, i.e., the time for peak neutron production). Similar to what was seen in Fig. 137.68, only small differences between κ_{QMD} and κ_{LILAC} simulations are observed for this mid-adiabat NIF design. The comparison of target performance is summarized in Table 137.VII, in which the differences in neutron-averaged ρR, T_i, pressure $\langle P \rangle_n$, hot-spot radius R_{hs}, hot-spot convergence ratio C_{hs}, neutron yield, and gain are all within ~2%.

Figure 137.71 illustrates the simulation results for a slightly lower adiabat ($\alpha \simeq 2.5$), high-convergence NIF design. Similar to Fig. 137.69 for the $\alpha = 2.2$ OMEGA implosion, Figs. 137.71(a)–137.71(d) plot (a) the pulse shape (total energy of 1.6 MJ),

Table 137.VII: Comparison of a mid-adiabat ($\alpha = 3.2$) NIF design simulated with κ_{LILAC} versus κ_{QMD}.

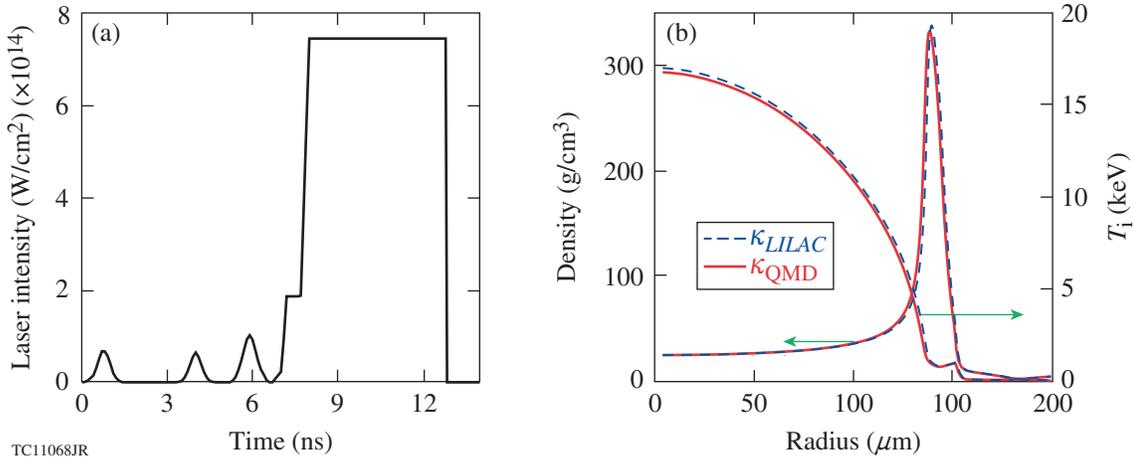|	κ_{LILAC}	κ_{QMD}
$\langle \rho R \rangle_n$	0.654 g/cm^2	0.655 g/cm^2
$\langle T_i \rangle_n$	12.2 keV	12.1 keV
$\langle P \rangle_n$	250 Gbar	248 Gbar
$\langle \rho \rangle_{peak}$	337.4 g/cm^3	331.8 g/cm^3
R_{hs}	91.4 μm	91.3 μm
C_{hs}	18.9	18.9
Yield	6.45×10^{18}	6.33×10^{18}
Gain	12.1	11.8

Figure 137.70
Similar to Fig. 137.68 but for a NIF-scale implosion: (a) The laser pulse shape for a mid-adiabat ($\alpha = 3.2$), 1.5-MJ direct-drive NIF design (the $\phi = 3460$-μm capsule consists of 220 μm of DT ice with a 30-μm-thick plastic ablator); (b) comparisons of the density and ion-temperature profiles at the peak compression for the two hydrodynamic runs using κ_{LILAC} (blue dashed lines) and κ_{QMD} (red solid lines), respectively. The effects of using different κ are small for such mid-adiabat designs.
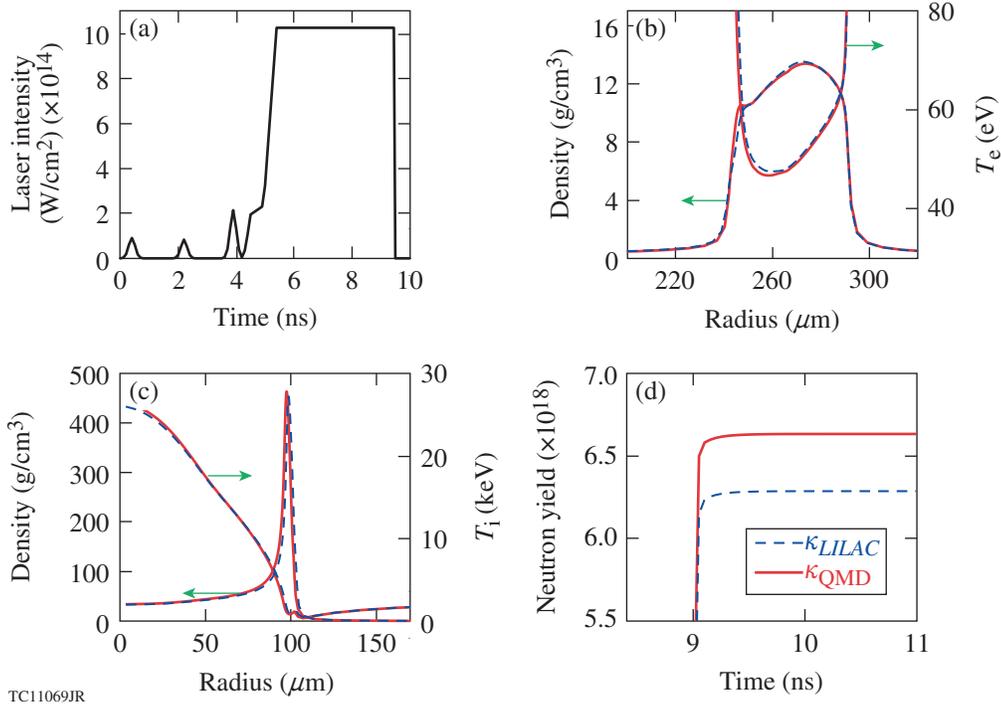

Figure 137.71
Tests on a high-implosion-velocity NIF design: (a) The laser pulse shape ($\alpha = 2.5$) has a total energy of 1.6 MJ (the $\phi = 3294$-μm capsule consists of 125 μm of DT ice with a 22-μm-thick plastic ablator). Panels (b) and (c) compare the density and temperature profiles at the beginning of the deceleration phase and at peak compression, respectively, for the two hydrodynamic simulations using κ_{LILAC} (blue dashed lines) and κ_{QMD} (red solid lines). The neutron yields as a function of time are plotted in panel (d) for the two cases. The use of κ_{QMD} modestly changes the 1-D prediction of implosion performance (~6%).

(b) the in-flight density and electron-temperature profiles at $t =$ 8.6 ns, (c) the bang-time density and ion-temperature profiles at $t = 8.91$ ns, and (d) the final neutron yield. Again, some slight differences in the electron temperature at the back surface of the shell can be seen in Fig. 137.71(b). The observables predicted by the two hydrodynamic simulations using κ_{QMD} in contrast to κ_{LILAC} are summarized in Table 137.VIII. Overall, a level of ~6% increase in target performance is seen in the κ_{QMD} simulation when compared to the standard κ_{LILAC} case.

Table 137.VIII: Comparison of a low-adiabat ($\alpha = 2.5$) NIF design simulated with κ_{LILAC} versus κ_{QMD}.

	κ_{LILAC}	κ_{QMD}
$\langle \rho R \rangle_n$	0.646 g/cm^2	0.661 g/cm^2
$\langle T_i \rangle_n$	20.8 keV	21.5 keV
$\langle P \rangle_n$	715 Gbar	763 Gbar
$\langle \rho \rangle_{peak}$	456.8 g/cm^3	466.9 g/cm^3
R_{hs}	56.2 μm	53.8 μm
C_{hs}	29.3	30.6
Yield	6.3×10^{18}	6.7×10^{18}
Gain	11.1	11.7

We further analyze the implosion dynamics of the NIF design shown in Fig. 137.71. The noticeable ρ/T_e differences at the back of the shell illustrated by Fig. 137.71(b) must come from the different shock dynamics in early stages of the implosion. To further explore the differences, in Fig. 137.72 we have plotted the DT plasma conditions at the shock transit stage. In Fig. 137.72(a), the density and temperature profiles are displayed for a snapshot at $t = 4.0$ ns. To clearly see the differences, we have plotted these profiles as a function of the simulation Lagrangian cell number. At this snapshot, the first shock [dashed circle in Fig. 137.63(a)] has propagated to near the back surface (at the 150th cell) of the DT ice layer. An interesting difference between two simulations can be clearly seen at the first shock front (near the 165th cell), in which the temperature front (at the 175th cell) predicted by the κ_{LILAC} simulation does *not* follow the density front of the shock. This occurs because the standard κ_{LILAC} significantly underestimates the thermal conductivity by an order of magnitude, for the shocked-DT plasma condition of $\rho_{DT} \simeq 1$ g/cm^2 and $T_e \simeq 1$ to 2 eV. The reduced thermal conductivity in κ_{LILAC} decreases the heat flow behind the shock front. On the contrary, the κ_{QMD} simulation (red solid lines) indicates the same shock-front location for both density and temperature, as expected. Differences in both density and temperature are also seen after the second

shock [near the 260th cell shown in Fig. 137.72(a)]. The κ_{LILAC} simulation predicts more "artificial" fluctuations in density and temperature after the second shock. Figure 137.72(b) shows another snapshot at $t = 4.8$ ns, when the first shock breaks out at the back of the DT ice layer into the DT gas. A large difference in electron-temperature profile is observed for the two simulations: the instant heat conduction in the κ_{QMD} case results in
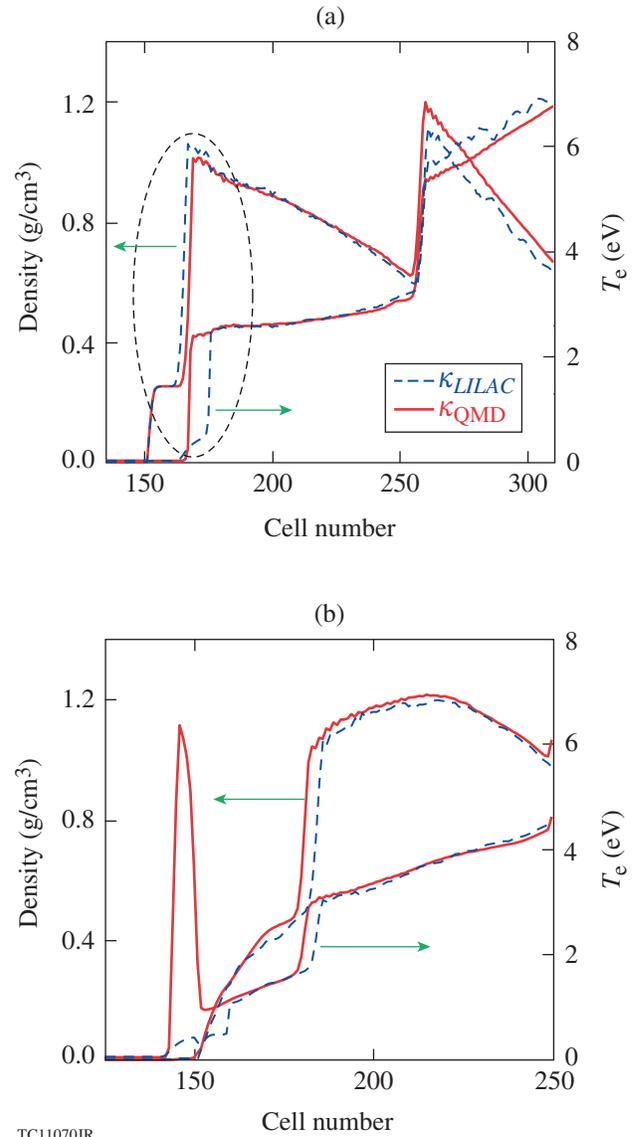

(a)

(b)

TC11070JR

Figure 137.72
The predicted shock conditions during the shock transit stage in the DT ice, for the NIF design plotted in Fig. 137.71. The density and electron temperature are plotted as a function of the Lagrangian cell numbers for times at (a) $t =$ 4.0 ns and (b) $t = 4.8$ ns. Again, the two cases of using κ_{LILAC} (blue dashed lines) and κ_{QMD} (red solid lines) are compared. The dashed circle highlights the first shock.

the immediate heating up of the releasing back surface, which is in contrast to the delayed heating in the κ_{LILAC} simulation. These different shock dynamics at the early stage of implosion cause the observable density–temperature variations late in the implosion, plotted in Fig. 137.71(b). This is the major contribution responsible for the final difference in target performance, which is discussed below.

Finally, the very low adiabat ($\alpha \simeq 1.7$) NIF design is examined in Fig. 137.73 and Table 137.IX. The implosion is designed to be driven by a 1.2-MJ pulse shape shown in Fig. 137.73(a), which has a ramping and low-intensity main pulse to avoid possible preheat from two-plasmon-decay–induced hot electrons.[64,65] The implosion velocity for this design is about 3.3×10^7 cm/s. Since the adiabat is so low that the DT-plasma conditions for the in-flight shell lie deeply within the more-degenerate and coupled regime, where κ_{QMD} is much higher than κ_{LILAC}, the effects of using κ_{QMD} are dramatically increased when compared to the higher-adiabat implosions discussed above. From Table 137.IX and Fig. 137.73, an ~20% variation in target performance (yield and gain) is observed in

the predictions of the two cases. Figure 137.73(b) shows that the simulation using κ_{QMD} predicts a lower electron-temperature profile for the back of the shell ($R \simeq 420$ μm). This results in a larger peak density of the shell and higher T_i at the bang time for the κ_{QMD} case, illustrated by Fig. 137.73(c), thereby leading to more neutron yields and gain.

Table 137.IX: Comparison of a very low adiabat ($\alpha = 1.7$) NIF design simulated with κ_{LILAC} versus κ_{QMD}.

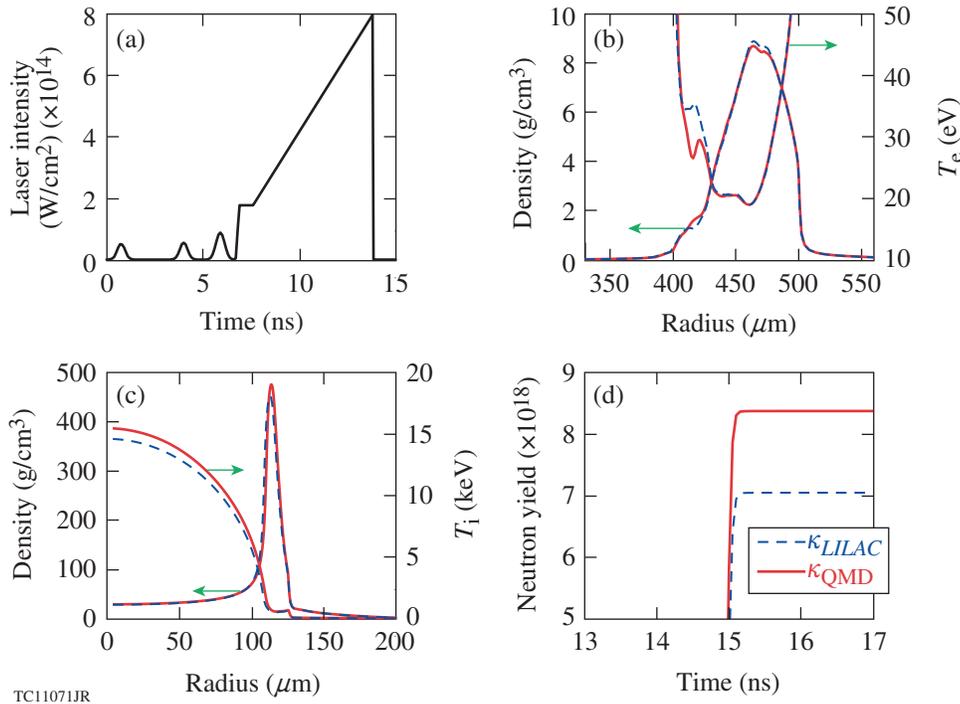|	κ_{LILAC}	κ_{QMD}
$\langle \rho R \rangle_n$	0.679 g/cm^2	0.69 g/cm^2
$\langle T_i \rangle_n$	13.1 keV	14.1 keV
$\langle P \rangle_n$	299 Gbar	335 Gbar
$\langle \rho \rangle_{peak}$	475.7 g/cm^3	495.1 g/cm^3
R_{hs}	80.9 μm	79.3 μm
C_{hs}	21.1	21.6
Yield	7.07×10^{18}	8.41×10^{18}
Gain	16.6	19.7

TC11071JR

Figure 137.73
Similar to Fig. 137.71 but for a relatively lower adiabat ($\alpha = 1.7$) and lower implosion velocity ($V_{imp} = 3.3 \times 10^7$ cm/s) NIF design: (a) The laser pulse shape has a total energy of 1.2 MJ and the $\phi = 3420$-μm capsule consists of 180 μm of DT ice with a 30-μm-thick plastic ablator. [(b),(c)] Comparison of the density and temperature profiles at the beginning of the deceleration phase and at the peak compression, respectively. (d) Comparison of the neutron yields for the two cases, which shows an ~20% variation in the 1-D predictions of target performance using κ_{LILAC} and κ_{QMD}.

To test the conventional speculation that κ_{QMD} affects mainly the hot-spot formation, we performed a "hybrid" simulation for this design by switching κ_{QMD} to the standard κ_{LILAC} during the target deceleration phase and burn ($t > 13.6$ ns). This hybrid simulation gives a total neutron yield of 9.29×10^{18} and a gain of 21.8. Comparing with the full κ_{QMD} simulation results ($Y = 8.41 \times 10^{18}$ and $G = 19.7$), the variation is modest with respect to the change from the full κ_{LILAC} simulation to the full κ_{QMD} case. This indicates that the major part of the κ_{QMD} effects on target performance comes from the shock dynamics during the early stage of the implosion, although the use of κ_{QMD} moderately decreases the target performance during the hot-spot formation.

Summary

For inertial confinement fusion applications, we have performed first-principles calculations of deuterium thermal conductivity in a wide range of densities and temperatures, using the quantum molecular dynamics method. For the density and temperature conditions in an imploding DT shell, the QMD-calculated thermal conductivity κ_{QMD} is higher by a factor of 3 to 10 than the hybrid Spitzer–Lee–More model κ_{LILAC} currently adopted in our hydrocodes. To test its effects on ICF implosions, we have fitted κ_{QMD} to a fifth-order polynomial function of Γ and θ and incorporated this fit into our hydrocodes. The hydrodynamic simulations of both OMEGA cryogenic DT implosions and direct-drive NIF designs have been performed using κ_{QMD}. Compared with the standard simulation results using κ_{LILAC}, we found the ICF implosion performance predicted by κ_{QMD} could vary by as much as ~20%. The lower the adiabat of the DT shell, the more the effects of κ_{QMD} are observed. Analyses of the implosion dynamics have identified that the shock-dynamic differences at an early stage of the implosion, predicted differently by κ_{QMD} versus κ_{LILAC}, predominantly contribute to the final variations of implosion performance (neutron yield and target gain). This is in contrast to the previous speculation that κ_{QMD} might affect ICF mainly during the hot-spot formation. The thermal conductivities of deuterium reported here, together with the established FPEOS tables[11,45] and opacity tables (future work) from such first-principles calculations, could provide complete physical information of fusion fuel at high-energy-density conditions for accurate ICF hydrodynamic simulations. The same strategy also applies for building self-consistent tables of ICF-relevant ablator materials. These efforts could increase the predictive capability of hydrodynamic modeling of ICF implosions.

Supplementary Material

Table 137.X: The thermal-conductivity (κ_{QMD}) table of deuterium for a wide range of densities.

Temperature T (K)	κ_{QMD} (W/m/K)
$\rho = 1.000$ g/cm^3	($r_S = 1.753$ bohr)
5,000	59.87±4.93
10,000	127.3±10.3
15,625	202.1±13.2
31,250	451.6±18.7
62,500	1199.6±49.6
95,250	2227.5±90.3
125,000	3281.4±139.0
181,825	6041.6±144.3
250,000	10491.2±203.1
$\rho = 1.963$ g/cm^3	($r_S = 1.4$ bohr)
5,000	239.77±21.7
10,000	374.07±34.46
15,625	492.57±43.67
31,250	$(1.00\pm0.04) \times 10^3$
62,500	$(2.17\pm0.09) \times 10^3$
95,250	$(3.68\pm0.21) \times 10^3$
125,000	$(5.17\pm0.25) \times 10^3$
181,825	$(8.41\pm0.37) \times 10^3$
250,000	$(1.30\pm0.02) \times 10^4$
400,000	$(2.32\pm0.02) \times 10^4$
$\rho = 2.452$ g/cm^3	($r_S = 1.3$ bohr)
5,000	345.5±39.5
10,000	499.2±47.6
15,625	676.5±41.6
31,250	$(1.21\pm0.08) \times 10^3$
62,500	$(2.74\pm0.11) \times 10^3$
95,250	$(4.38\pm0.18) \times 10^3$
125,000	$(6.26\pm0.29) \times 10^3$
181,825	$(1.00\pm0.04) \times 10^4$
250,000	$(1.53\pm0.04) \times 10^4$
400,000	$(2.79\pm0.05) \times 10^4$

Table 137.X (continued).

Temperature T (K)	κ_{QMD} (W/m/K)
ρ = 3.118 g/cm^3	(r_S = 1.2 bohr)
5,000	472.5±54.6
10,000	745.7±76.2
15,625	953.7±72.2
31,250	$(1.61\pm0.10) \times 10^3$
62,500	$(3.55\pm0.20) \times 10^3$
95,250	$(5.53\pm0.25) \times 10^3$
125,000	$(7.61\pm0.30) \times 10^3$
181,825	$(1.24\pm0.04) \times 10^4$
250,000	$(1.85\pm0.05) \times 10^4$
400,000	$(3.47\pm0.08) \times 10^4$
ρ = 4.048 g/cm^3	(r_S = 1.1 bohr)
5,000	778.8±83.3
10,000	$(1.03\pm0.08) \times 10^3$
15,625	$(1.36\pm0.12) \times 10^3$
31,250	$(2.12\pm0.05) \times 10^3$
62,500	$(4.48\pm0.22) \times 10^3$
95,250	$(7.17\pm0.28) \times 10^3$
125,000	$(9.75\pm0.52) \times 10^3$
181,825	$(1.51\pm0.06) \times 10^4$
250,000	$(2.32\pm0.08) \times 10^4$
400,000	$(4.36\pm0.12) \times 10^4$
ρ = 5.388 g/cm^3	(r_S = 1.0 bohr)
5,000	$(1.19\pm0.17) \times 10^3$
10,000	$(1.41\pm0.15) \times 10^3$
15,625	$(1.84\pm0.27) \times 10^3$
31,250	$(2.76\pm0.32) \times 10^3$
62,500	$(5.60\pm0.25) \times 10^3$
95,250	$(9.33\pm0.42) \times 10^3$
125,000	$(1.27\pm0.06) \times 10^4$
181,825	$(2.01\pm0.06) \times 10^4$
250,000	$(2.91\pm0.11) \times 10^4$
400,000	$(5.53\pm0.17) \times 10^4$
500,000	$(9.48\pm0.13) \times 10^4$

Table 137.X (continued).

Temperature T (K)	κ_{QMD} (W/m/K)
ρ = 7.391 g/cm^3	(r_S = 0.9 bohr)
5,000	$(2.00\pm0.37) \times 10^3$
10,000	$(2.24\pm0.21) \times 10^3$
15,625	$(2.67\pm0.28) \times 10^3$
31,250	$(4.14\pm0.33) \times 10^3$
62,500	$(7.59\pm0.59) \times 10^3$
95,250	$(1.30\pm0.07) \times 10^4$
125,000	$(1.75\pm0.10) \times 10^4$
181,825	$(2.61\pm0.08) \times 10^4$
250,000	$(3.80\pm0.17) \times 10^4$
400,000	$(6.94\pm0.23) \times 10^4$
500,000	$(9.52\pm0.33) \times 10^4$
ρ = 10.000 g/cm^3	(r_S = 0.814 bohr)
5,000	$(3.01\pm0.48) \times 10^3$
10,000	$(3.34\pm0.55) \times 10^3$
15,625	$(3.77\pm0.43) \times 10^3$
31,250	$(5.74\pm0.46) \times 10^3$
62,500	$(9.65\pm0.69) \times 10^3$
95,250	$(1.66\pm0.12) \times 10^4$
125,000	$(2.32\pm0.13) \times 10^4$
181,825	$(3.40\pm0.19) \times 10^4$
250,000	$(4.78\pm0.29) \times 10^4$
400,000	$(8.37\pm0.32) \times 10^4$
500,000	$(1.24\pm0.04) \times 10^5$
ρ = 15.709 g/cm^3	(r_S = 0.8 bohr)
10,000	$(7.29\pm0.70) \times 10^3$
15,625	$(7.57\pm0.80) \times 10^3$
31,250	$(1.20\pm0.09) \times 10^4$
62,500	$(1.99\pm0.11) \times 10^4$
95,250	$(2.78\pm0.17) \times 10^4$
125,000	$(3.50\pm0.17) \times 10^4$
181,825	$(5.24\pm0.21) \times 10^4$
250,000	$(7.50\pm0.33) \times 10^4$
400,000	$(1.34\pm0.05) \times 10^5$
500,000	$(1.80\pm0.04) \times 10^5$
1,000,000	$(3.79\pm0.11) \times 10^5$

Table 137.X (continued).

Temperature T (K)	κ_{QMD} (W/m/K)
$\rho = 24.945$ g/cm^3	($r_S = 0.6$ bohr)
15,625	$(1.49\pm0.15) \times 10^4$
31,250	$(1.71\pm0.13) \times 10^4$
62,500	$(3.18\pm0.21) \times 10^4$
95,250	$(4.24\pm0.27) \times 10^4$
125,000	$(5.31\pm0.27) \times 10^4$
181,825	$(7.06\pm0.49) \times 10^4$
250,000	$(9.95\pm0.35) \times 10^4$
400,000	$(1.68\pm0.07) \times 10^5$
500,000	$(2.19\pm0.11) \times 10^5$
1000,000	$(5.63\pm0.21) \times 10^5$
$\rho = 43.105$ g/cm^3	($r_S = 0.5$ bohr)
31,250	$(3.09\pm0.33) \times 10^4$
62,500	$(5.14\pm0.40) \times 10^4$
95,250	$(7.36\pm0.78) \times 10^4$
125,000	$(8.82\pm0.64) \times 10^4$
181,825	$(1.17\pm0.08) \times 10^5$
250,000	$(1.44\pm0.15) \times 10^5$
400,000	$(2.46\pm0.08) \times 10^5$
500,000	$(3.14\pm0.24) \times 10^5$
1,000,000	$(7.62\pm0.28) \times 10^5$
$\rho = 84.190$ g/cm^3	($r_S = 0.4$ bohr)
31,250	$(7.72\pm0.98) \times 10^4$
62,500	$(7.52\pm0.64) \times 10^4$
95,250	$(1.21\pm0.15) \times 10^5$
125,000	$(1.64\pm0.17) \times 10^5$
181,825	$(2.03\pm0.27) \times 10^5$
250,000	$(2.65\pm0.33) \times 10^5$
400,000	$(3.74\pm0.35) \times 10^5$
500,000	$(4.66\pm0.24) \times 10^5$
1,000,000	$(1.15\pm0.06) \times 10^6$
2,000,000	$(3.12\pm0.05) \times 10^6$

Table 137.X (continued).

Temperature T (K)	κ_{QMD} (W/m/K)
$\rho = 199.561$ g/cm^3	($r_S = 0.3$ bohr)
125,000	$(4.93\pm0.21) \times 10^5$
181,825	$(6.18\pm0.24) \times 10^5$
250,000	$(8.19\pm0.20) \times 10^5$
400,000	$(1.25\pm0.05) \times 10^6$
500,000	$(1.52\pm0.06) \times 10^6$
1,000,000	$(2.86\pm0.09) \times 10^6$
2,000,000	$(6.38\pm0.09) \times 10^6$
4,000,000	$(1.57\pm0.10) \times 10^7$
$\rho = 673.518$ g/cm^3	($r_S = 0.2$ bohr)
250,000	$(2.43\pm0.17) \times 10^6$
400,000	$(3.18\pm0.24) \times 10^6$
500,000	$(3.76\pm0.26) \times 10^6$
1,000,000	$(7.34\pm0.35) \times 10^6$
2,000,000	$(1.44\pm0.07) \times 10^7$
4,000,000	$(3.33\pm0.06) \times 10^7$
8,000,000	$(8.92\pm0.08) \times 10^7$

REFERENCES

1. J. Nuckolls *et al.*, Nature **239**, 139 (1972); S. Atzeni and J. Meyer-ter-Vehn, *The Physics of Inertial Fusion: Beam Plasma Interaction, Hydrodynamics, Hot Dense Matter*, International Series of Monographs on Physics (Clarendon Press, Oxford, 2004).

2. J. D. Lindl, Phys. Plasmas **2**, 3933 (1995).

3. C. Cherfils-Clérouin *et al.*, J. Phys.: Conf. Ser. **244**, 022009 (2010).

4. R. L. McCrory, R. Betti, T. R. Boehly, D. T. Casey, T. J. B. Collins, R. S. Craxton, J. A. Delettrez, D. H. Edgell, R. Epstein, J.A. Frenje, D. H. Froula, M. Gatu-Johnson, V. Yu. Glebov, V. N. Goncharov, D. R. Harding, M. Hohenberger, S. X. Hu, I. V. Igumenshchev, T. J. Kessler, J. P. Knauer, C.K. Li, J. A. Marozas, F. J. Marshall, P. W. McKenty, D. D. Meyerhofer, D. T. Michel, J. F. Myatt, P. M. Nilson, S. J. Padalino, R.D. Petrasso, P. B. Radha, S. P. Regan, T. C. Sangster, F. H. Séguin, W. Seka, R. W. Short, A. Shvydky, S. Skupsky, J. M. Soures, C. Stoeckl, W. Theobald, B. Yaakobi, and J. D. Zuegel, Nucl. Fusion **53**, 113021 (2013).

5. D. D. Meyerhofer, R. L. McCrory, R. Betti, T. R. Boehly, D. T. Casey, T. J. B. Collins, R. S. Craxton, J. A. Delettrez, D. H. Edgell, R. Epstein, K. A. Fletcher, J. A. Frenje, Y. Yu. Glebov, V. N. Goncharov, D. R. Harding, S. X. Hu, I. V. Igumenshchev, J. P. Knauer, C. K. Li, J. A. Marozas, F. J. Marshall, P. W. McKenty, P. M. Nilson, S. P. Padalino, R. D. Petrasso, P. B. Radha, S. P. Regan, T. C. Sangster, F. H. Séguin, W. Seka, R. W. Short, D. Shvarts, S. Skupsky, J. M. Soures, C. Stoeckl, W. Theobald, and B. Yaakobi, Nucl. Fusion **51**, 053010 (2011).

6. V. N. Goncharov, T. C. Sangster, T. R. Boehly, S. X. Hu, I. V. Igumenshchev, F. J. Marshall, R. L. McCrory, D. D. Meyerhofer, P. B. Radha, W. Seka, S. Skupsky, C. Stoeckl, D. T. Casey, J. A. Frenje, and R. D. Petrasso, Phys. Rev. Lett. **104**, 165001 (2010).

7. M. C. Herrmann, M. Tabak, and J. D. Lindl, Nucl. Fusion **41**, 99 (2001).

8. C. D. Zhou and R. Betti, Phys. Plasmas **15**, 102707 (2008).

9. S. X. Hu, V. A. Smalyuk, V. N. Goncharov, J. P. Knauer, P. B. Radha, I. V. Igumenshchev, J. A. Marozas, C. Stoeckl, B. Yaakobi, D. Shvarts, T. C. Sangster, P. W. McKenty, D. D. Meyerhofer, S. Skupsky, and R. L. McCrory, Phys. Rev. Lett. **100**, 185003 (2008).

10. J. Clérouin and J.-F. Dufrêche, Phys. Rev. E **64**, 066406 (2001); L. Caillabet, S. Mazevet, and P. Loubeyre, Phys. Rev. B **83**, 094101 (2011).

11. S. X. Hu, B. Militzer, V. N. Goncharov, and S. Skupsky, Phys. Rev. B **84**, 224109 (2011).

12. M. A. Morales *et al.*, High Energy Density Phys. **8**, 5 (2012).

13. S. Hamel, L. X. Benedict, P. M. Celliers, M. A. Barrios, T. R. Boehly, G. W. Collins, T. Döppner, J. H. Eggert, D. R. Farley, D. G. Hicks, J. L. Kline, A. Lazicki, S. LePape, A. J. Mackinnon, J. D. Moody, H. F. Robey, E. Schwegler, and P. A. Sterne, Phys. Rev. B **86**, 094113 (2012); P. Loubeyre, S. Brygoo, J. Eggert, P. M. Celliers, D. K. Spaulding, J. R. Rygg, T. R. Boehly, G. W. Collins, and R. Jeanloz, Phys. Rev. B **86**, 144115 (2012).

14. J. Vorberger, D. O. Gericke, and W. D. Kraeft, High Energy Density Phys. **9**, 448 (2013).

15. C. Wang and P. Zhang, Phys. Plasmas **20**, 092703 (2013).

16. V. V. Karasiev *et al.*, Phys. Rev. B **88**, 161108 (2013).

17. B. Militzer and D. M. Ceperley, Phys. Rev. Lett. **85**, 1890 (2000); B. Militzer *et al.*, Phys. Rev. Lett. **87**, 275502 (2001).

18. J. M. McMahon *et al.*, Rev. Mod. Phys. **84**, 1607 (2012).

19. L. Collins *et al.*, Phys. Rev. E **52**, 6202 (1995).

20. H. Brysk, P. M. Campbell, and P. Hammerling, Plasma Phys. **17**, 473 (1975).

21. L. Spitzer, Jr. and R. Härm, Phys. Rev. **89**, 977 (1953).

22. J. Daligault and G. Dimonte, Phys. Rev. E **79**, 056403 (2009).

23. L. X. Benedict *et al.*, Phys. Rev. Lett. **102**, 205004 (2009).

24. B. Xu and S. X. Hu, Phys. Rev. E **84**, 016408 (2011).

25. L. X. Benedict *et al.*, Phys. Rev. E **86**, 046406 (2012).

26. C. Blancard, J. Clérouin, and G. Faussurier, High Energy Density Phys. **9**, 247 (2013).

27. W. B. Hubbard, Astrophys. J. **146**, 858 (1966).

28. Y. T. Lee and R. M. More, Phys. Fluids **27**, 1273 (1984).

29. S. Ichimaru and S. Tanaka, Phys. Rev. A **32**, 1790 (1985); H. Kitamura and S. Ichimaru, Phys. Rev. E **51**, 6004 (1995).

30. D. A. Liberman, Phys. Rev. B **20**, 4981 (1979).

31. B. Wilson *et al.*, J. Quant. Spectrosc. Radiat. Transf. **99**, 658 (2006).

32. G. Faussurier *et al.*, Phys. Plasmas **17**, 052707 (2010); J. Clérouin *et al.*, Phys. Rev. E **82**, 046402 (2010).

33. J. G. Clérouin and S. Bernard, Phys. Rev. E **56**, 3534 (1997).

34. L. A. Collins *et al.*, Phys. Rev. B **63**, 184110 (2001).

35. M. P. Desjarlais, Phys. Rev. B **68**, 064204 (2003).

36. S. A. Bonev, B. Militzer, and G. Galli, Phys. Rev. B **69**, 014101 (2004).

37. J. D. Kress *et al.*, Phys. Rev. E **82**, 036404 (2010).

38. V. Recoules *et al.*, Phys. Rev. Lett. **102**, 075002 (2009).

39. F. Lambert *et al.*, Phys. Plasmas **18**, 056306 (2011).

40. D. E. Hanson *et al.*, Phys. Plasmas **18**, 082704 (2011).

41. B. Holst, M. French, and R. Redmer, Phys. Rev. B **83**, 235120 (2011).

42. C. E. Starrett *et al.*, Phys. Plasmas **19**, 102709 (2012).

43. C. Wang *et al.*, Phys. Rev. E **88**, 013106 (2013).

44. For details of the *ABINIT* code, please refer to http://www.abinit.org/.

45. S. X. Hu, B. Militzer, V. N. Goncharov, and S. Skupsky, Phys. Rev. Lett. **104**, 235003 (2010).

46. R. Kubo, J. Phys. Soc. Jpn. **12**, 570 (1957); D. A. Greenwood, Proc. Phys. Soc. Lond. **71**, 585 (1958).

47. J. Delettrez, R. Epstein, M. C. Richardson, P. A. Jaanimagi, and B. L. Henke, Phys. Rev. A **36**, 3926 (1987).

48. I. Kwon, J. D. Kress, and L. A. Collins, Phys. Rev. B **50**, 9118 (1994).

49. M. P. Desjarlais, J. D. Kress, and L. A. Collins, Phys. Rev. E **66**, 025401 (2002).

50. B. Holst, R. Redmer, and M. P. Desjarlais, Phys. Rev. B **77**, 184201 (2008).

51. G. Kresse and J. Hafner, Phys. Rev. B **47**, 558 (1993).

52. G. Kresse and J. Hafner, Phys. Rev. B **49**, 14,251 (1994); G. Kresse and J. Furthmüller, Phys. Rev. B **54**, 11,169 (1996).

53. G. Kresse and D. Joubert, Phys. Rev. B **59**, 1758 (1999).

54. G. Kresse, University of Vienna, private communication (2013).

55. P. M. Celliers *et al.*, Phys. Rev. Lett. **84**, 5564 (2000).

56. T. R. Boehly, D. H. Munro, P. M. Celliers, R. E. Olson, D. G. Hicks, V. N. Goncharov, G. W. Collins, H. F. Robey, S. X. Hu, J. A. Marozas, T. C. Sangster, O. L. Landen, and D. D. Meyerhofer, Phys. Plasmas **16**, 056302 (2009).

57. T. R. Boehly, V. N. Goncharov, W. Seka, S. X. Hu, J. A. Marozas, D. D. Meyerhofer, P. M. Celliers, D. G. Hicks, M. A. Barrios, D. Fratanduono, and G. W. Collins, Phys. Plasmas **18**, 092706 (2011).

58. T. R. Boehly, V. N. Goncharov, W. Seka, M. A. Barrios, P. M. Celliers, D. G. Hicks, G. W. Collins, S. X. Hu, J. A. Marozas, and D. D. Meyerhofer, Phys. Rev. Lett. **106**, 195005 (2011).

59. L. A. Collins, J. D. Kress, and D. E. Hanson, Phys. Rev. B **85**, 233101 (2012).

60. R. C. Malone, R. L. McCrory, and R. L. Morse, Phys. Rev. Lett. **34**, 721 (1975).

61. S. X. Hu, V. Smalyuk, V. N. Goncharov, S. Skupsky, T. C. Sangster, D. D. Meyerhofer, and D. Shvarts, Phys. Rev. Lett. **101**, 055002 (2008).

62. S. X. Hu, P. B. Radha, J. A. Marozas, R. Betti, T. J. B. Collins, R. S. Craxton, J. A. Delettrez, D. H. Edgell, R. Epstein, V. N. Goncharov, I. V. Igumenshchev, F. J. Marshall, R. L. McCrory, D. D. Meyerhofer, S. P. Regan, T. C. Sangster, S. Skupsky, V. A. Smalyuk, Y. Elbaz, and D. Shvarts, Phys. Plasmas **16**, 112706 (2009).

63. S. X. Hu, V. N. Goncharov, P. B. Radha, J. A. Marozas, S. Skupsky, T. R. Boehly, T. C. Sangster, D. D. Meyerhofer, and R. L. McCrory, Phys. Plasmas **17**, 102706 (2010).

64. D. H. Froula, B. Yaakobi, S. X. Hu, P.-Y. Chang, R. S. Craxton, D. H. Edgell, R. Follett, D. T. Michel, J. F. Myatt, W. Seka, R. W. Short, A. Solodov, and C. Stoeckl, Phys. Rev. Lett. **108**, 165003 (2012).

65. S. X. Hu, D. T. Michel, D. H. Edgell, D. H. Froula, R. K. Follett, V. N. Goncharov, J. F. Myatt, S. Skupsky, and B. Yaakobi, Phys. Plasmas **20**, 032704 (2013).